Boron oxynitride quantum dots for CO$_2$ photoreduction

Ravi B. Shankar,[a] Elan D. R. Mistry,[b] Mahmoud Ardakani[c] and Camille Petit[a,*]

Photocatalytically active boron oxynitride quantum dots (BNO QDs) were produced *via* a bottom-up hydrothermal synthesis. This is the first demonstration of BN-based quantum dots being employed as photocatalysts. The material facilitates CO$_2$ photoreduction, with evolution rates and quantum efficiencies exceeding those for P25 TiO$_2$, the benchmark catalyst in the field.

Quantum dots (QDs) represent a family of 0D materials, typically exhibiting a lateral size less than 20 nm,[1] which encompass a broad spectrum of chemical, optoelectronic, magnetic and catalytic properties.[2, 3] QDs exhibit higher surface-to-volume ratios compared to bulk materials, as well as a large number of dangling bonds, which makes them highly sensitive to surface defects and adsorbate interactions.[4] This has facilitated a range of applications including, but not restricted to, drug delivery, sensing and catalysis. QDs often exhibit strikingly different electronic and photochemical behaviour in contrast to their bulk counterparts. This is attributed to edge effects and spatial quantum confinement phenomena, arising at sizes less than the Bohr radii of charge carriers. This results in larger HOMO-LUMO gaps and discretised electronic states.[5] However, the confined size of QDs can facilitate efficient charge separation due to the shorter bulk-to-surface migration distance for the exciton pair.[6] This efficient charge separation, coupled with tunable chemistry and optoelectronic properties, has made several organic and inorganic QDs attractive alternatives to bulk materials for photocatalysis.[7-12] Aside from carbon-based QDs, the majority of QDs as photocatalysts present the problem of toxicity and/or usage of non-abundant heavy metals (e.g. CdX: X = S, Se, Te and PbS).[13, 14] Like carbon-based QDs, boron nitride (BN) and BN-based QDs have garnered interest owing to their non-toxicity[15] and high degree of tunability. Tailoring the size, morphology, composition and edge functionalisation have been shown to alter the optical, magnetic and electronic properties of BN-based QDs.[16-18] The primary applications of BN QDs in literature so far include: photoluminescence[19-21], sensing[22, 23] and bioimaging.[24, 25] Yang *et al*.[26] recently utilised BN-based QDs to enhance exciton dissociation and charge transfer in decorated graphitic carbon nitride for visible light-driven oxygen activation. However, the photoactivity from the BN-based QDs as standalone materials was not assessed.[27] There have been no reports to date of BN-based QDs being able to function as stand-alone photocatalysts without the aid of cocatalysts, namely due to a large band gap (~5.0 – 6.0 eV in BN QDs[1]). The work described herein addresses this gap and provides a step-change addition to the current BN-based photocatalysts family.[28, 29]

To lower the band gap of the BN-based QDs, we employed oxygen doping in a bottom-up hydrothermal synthesis route (Fig. 1). Oxygen doping has recently been shown to be a band gap narrowing strategy in bottom-up syntheses of BN materials.[30] The resulting product is termed boron oxynitride (BNO), owing to the significant proportion of interior-substituted oxygen atoms, to distinguish from other BN materials. In short, an aqueous solution of boric acid and hexamethylenetetramine (HMTA) was reacted in an autoclave at 200 °C for 18 hours (Fig. 1). A tertiary amine (HMTA) was used as the nitrogen precursor instead of commonly used primary amines (e.g. melamine) to promote oxygen doping owing to the higher reaction energy barrier.[30] After cooling to room temperature, the reaction mixture was filtered using an ultrafiltration

membrane (0.22 µm) to remove larger particles. A yellow solution of BNO QDs were obtained (inset Fig. 1). The solution was evaporated off at 90 °C in a drying oven to obtain a yellow powder (inset Fig. 1), which we used for characterisation and photocatalytic testing.

We first characterised the structure and morphology using high resolution transmission electron microscopy (HRTEM) to gain insight
into the size distribution of the BNO QDs (Fig. 2). From Figs. 2a and 2b, the BNO QDs exhibit spherical morphology and are mainly distributed in the 2 – 5 nm range, with an average lateral size of approximately 3 nm (as determined by ImageJ).[31] This is in agreement with previous literature reports.[19, 26] As illustrated in the inset of Fig. 2a, the dark dot shows clear lattice fringes of 0.34 nm, corresponding to an interplanar d(002)-spacing.[32]
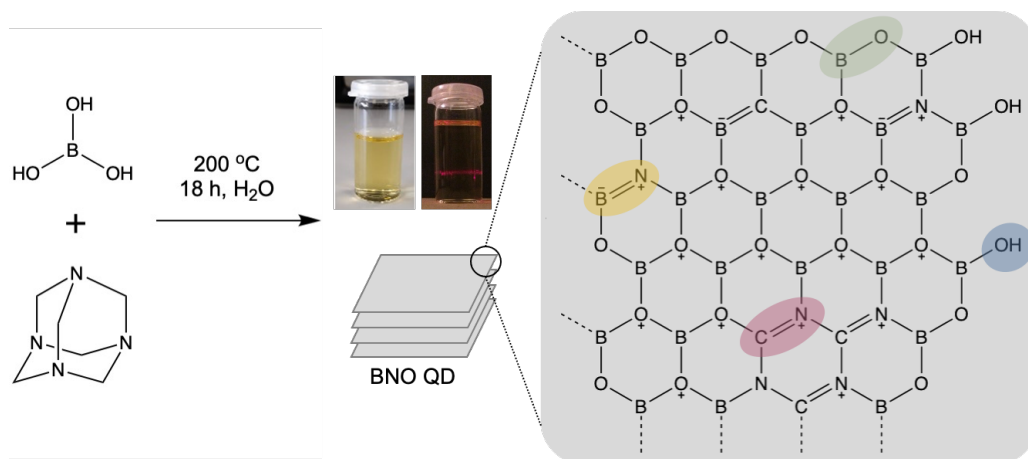

Fig. 1 Synthesis of boron oxynitride quantum dots (BNO QDs) *via* a bottom-up hydrothermal synthesis using boric acid and hexamethylenetetramine precursors. The structure shown on the right is a representation of part of a layer of the obtained BNO QDs. The insets show pictures of the BNO QDs aqueous solution, including visualisation of the Tyndall effect.

Typical XRD patterns for BN materials with characteristic peaks at 2θ values of 26° and 44°, corresponding to the (002) and (100) planes were observed (Fig. 2c).[33] BNO QDs exhibited a surface area of 2 m^2/g, as opposed to 49 m^2/g for TiO_2 P25 (Fig. S1). We next analysed the bonding types and chemical composition of the BNO QDs using Fourier transform infrared spectroscopy (FT-IR) and X-ray photoelectron spectroscopy (XPS) (Figs. 3 and S2). The sample exhibits the two characteristic IR bands of BN at ~1250 cm^{-1} (in-plane B-N transverse stretching) and ~750 cm^{-1} (out-of-plane B-N-B bending) (Fig. 3a).[34] We attribute the weaker band at ~1000 cm^{-1} to B-O bonds arising from interior substituted oxygen atoms.[29, 30] A broad O-H peak at ~3200 cm^{-1} is observed, highlighting edge hydroxide functionalisation and termination of the BNO QDs.[35, 36] The bands at ~930 cm^{-1} and ~1200 cm^{-1} likely correspond to C-H and C-N/C-O bonds, respectively.[37] The presence of carbon in BN QDs is common and has been reported.[19, 36, 38] Compared to hydro-/solvothermal routes, bottom-up pyrolytic syntheses of BN, more so under the presence of ammonia[39], aid the removal of carbon from the end product.[28, 29] To gain further insight into the relative atomic surface composition and chemical states of the elements, we collected high resolution core level B 1s, C 1s, N 1s and O 1s spectra through XPS. In addition to B (39 at.%), a significant proportion of oxygen atoms (~50 at. %) was detected, the majority of which seems involved in B-O bonds (B 1s: 194.0 eV, O 1s: 533.1 eV). The peaks at 191.0/193.0 eV and 398.5 eV and 398.5 eV in the B 1s and N 1s spectra, respectively, likely belong to B-N/B-O_x-N_{3-x} bonds (Fig. S2).[40] We assign the C 1s peak at 286.3 eV to C-N/C-O bonds, in agreement with the FT-IR

spectrum in Fig. 3a.[25] We link the main N 1s peak at 402.5 eV to C-N. We used the bonding patterns derived from the FT-IR spectrum and XPS to construct the proposed structure of the BNO QDs in Fig. 1.

Next, we probed the optoelectronic properties of the BNO QDs through UV-vis diffuse reflectance spectroscopy (UV-Vis DRS). The absorption edge is ~ 355 nm (inset of Fig. 3c). From the Tauc plot of the transformed Kubelka-Munk function against photon energy (Fig. 3c), the BNO QDs exhibits a UV-range band gap of 3.50 eV. We consider BNO QDs as direct band-gap semiconductors based on literature.[41]
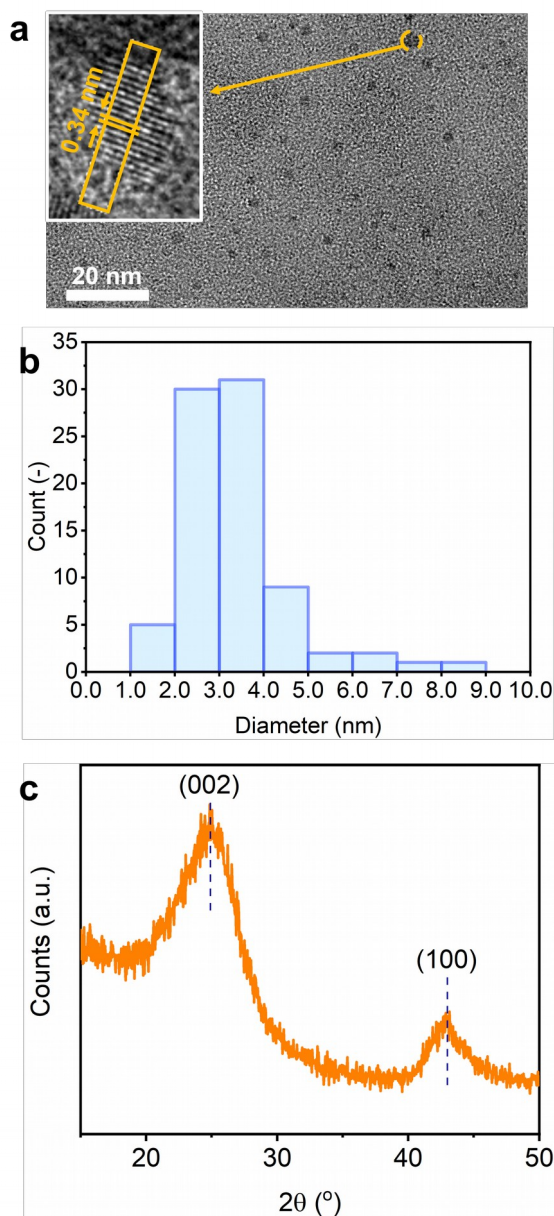

Fig. 2 Structure and morphology of the BNO QDs. (a) HRTEM image of the BNO QDs highlighting the spherical morphology (inset – lattice fringes). (b) Histogram of size distribution of BNO QDs as determined based on HRTEM images. (c) Powder XRD pattern of the BNO QDs with the characteristic (002) and (100) peaks highlighted.

We followed the same methodology as in a previous study[29] to determine the band structure of the BNO QDs by measuring the valence band offset (ΔE_{VB}) and work function (Φ) through XPS measurements (Fig. S3). We note here that since the charge carriers are bound and trapped in a

potential well, the energies relative to absolute vacuum are negative. Hence, the work function (Φ) and valence band offset (ΔE_{VB}) take negative values relative to absolute vacuum based on the notation outlined in our previous study.[29] The BNO QDs exhibited a valence band offset of -3.10 eV and a work function of -3.90 eV (Fig. S3). By combining this data with the optical band gaps determined in Fig. 3c, we determine the conduction and valence bands to be -3.50 eV and -7.00 eV. The complete band structures for the BNO QDs on the absolute energy scale vs. vacuum, with the redox potentials for CO_2/CO and H^+/H_2 vs. SHE at pH = 0 are presented in Fig. 3d. This is the first time the band structure for any type of BN QD is reported. The conduction and valence bands for the BNO QDs straddle the redox potentials for the CO_2 photoreduction system, which is imperative for the material to be able to thermodynamically facilitate the reaction. The thermodynamic overpotential for the CO_2 photoreduction reaction is approximately 1 V (Fig. 3d). We observe that the separation between the Fermi level (E_F) and conduction band is smaller than that with the valence band (Fig. 3d). This suggests that the BNO QDs exhibit n-type character, which is desirable for CO_2 photoreduction.

Next, we tested the BNO QDs for the gas phase photoreduction (or CO_2 hydrogenation) of CO_2, under UV-vis irradiation, in a simple gas/solid phase set-up under ambient conditions without the presence of a co-catalyst.
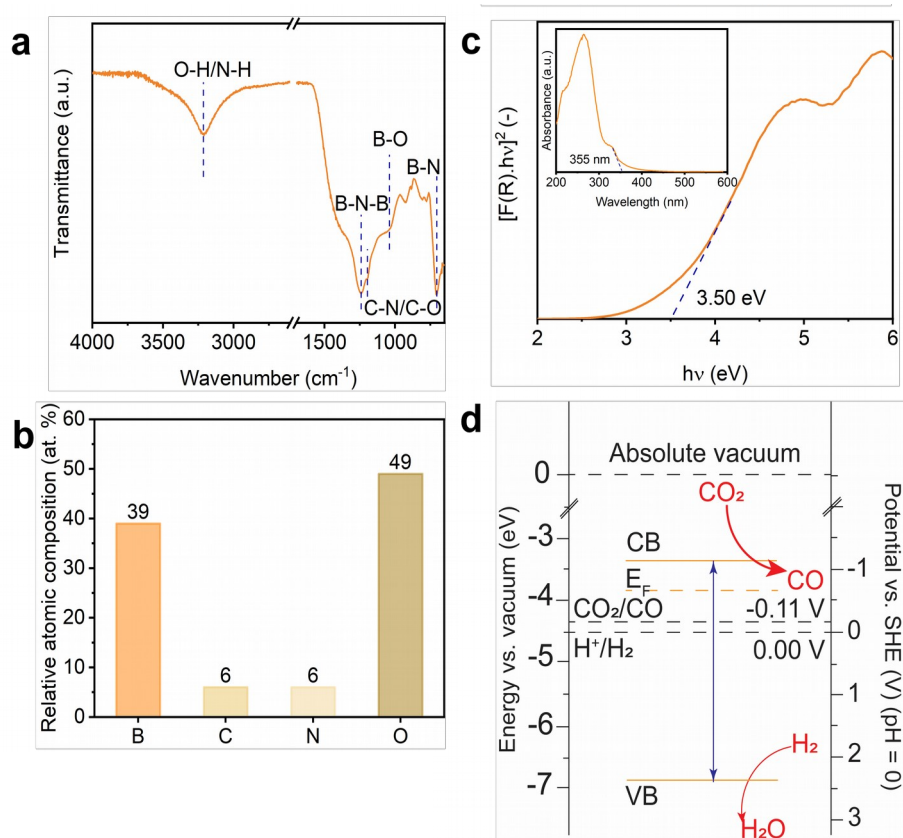

Fig. 3 Chemical and optoelectronic properties of the BNO QDs. (**a**) FT-IR spectrum for the BNO QDs with the bands highlighted. (**b**) Relative atomic composition of the BNO QDs as obtained from XPS. (**c**) Tauc plot of Kubelka-Munk function against photon energy (inset – absorption spectrum of BNO QDs) (**d**) Band structure for BNO QDs on the absolute energy scale vs. vacuum with the conduction and valence bands, with the redox potentials for CO_2/CO and H^+/H_2 *vs.* SHE at pH = 0 illustrated.

The photocatalytic output was compared to that of P25 TiO_2. P25 TiO_2 is a benchmark commercial material in the field, which enables comparison with other groups' work, despite differences in

experimental set-ups.[42] We used the same mass of catalyst, sample preparation and reaction conditions for both the BNO QDs and P25 TiO_2 (see Section S2). The lamp intensity spectra is presented in Fig. S4. For both materials, after an irradiation time of 3 hours, CO was observed as the major product, with comparatively smaller quantities of CH_4 detected. Under these conditions, the BNO QDs drove the photoreduction of CO_2 with an average specific CO production rate of 44.9 μ mol g^{-1} h^{-1} (Fig. 4a) and a quantum efficiency (QE) of 0.02 % across the UV-vis spectrum (270 – 900 nm), which was an order of magnitude higher than that of P25 TiO_2 (average CO production rate of 8.53 μ mol g^{-1} h^{-1} and QE of 1.2 x 10^{-3}) (Tables S1 and S2). The same trend amongst the materials is also observed with regard to the minor product, CH_4 (Fig. 4a and Table S1). The performance of the materials per available material surface area, as well as per irradiated surface area, is reported in Table S2.
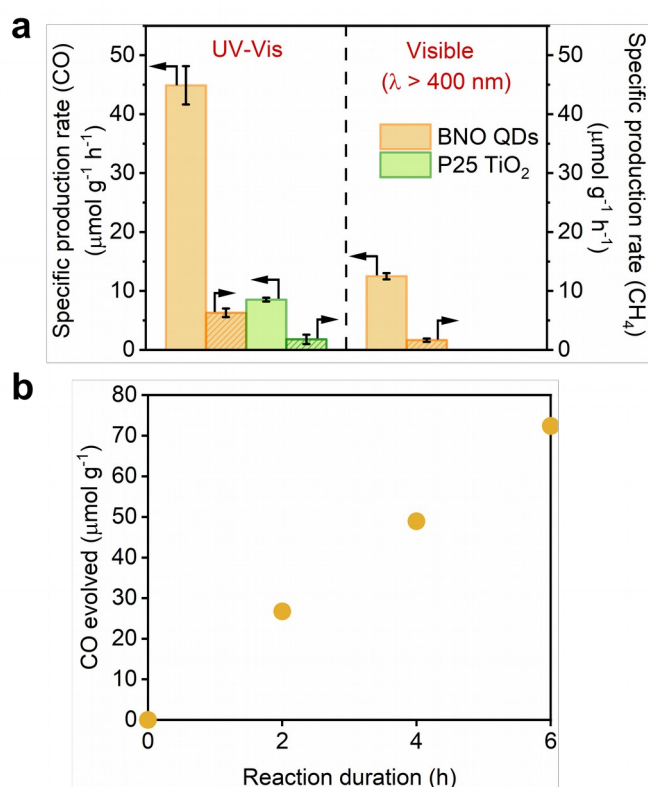

Fig. 4 Photocatalytic testing of the BNO QD sample. (**a**) Specific production rate of CO and CH_4 for BNO QDs, compared to P25 TiO_2, under UV-vis irradiation and H_2 as the sacrificial agent (300 W Xe arc lamp, 9.5 cm distance from catalyst to lamp source, 5 hours, 25 °C). Intensity at the catalyst surface was 1850 ± 17 W m^{-2}. (**b**) Kinetic study illustrating photocatalytic CO evolution from the BNO QDs as a function of time under UV-Vis irradiation (same lamp and reactor settings as before).

We confirmed the origin of CO isotopic labelling experiments using $^{13}CO_2$. Aside from $^{13}CO_2$ being used as the feed gas in tandem with H_2 as the sacrificial agent, we maintained the same catalyst preparation method and reaction conditions from the original system. The gas chromatograms corresponding to the ^{13}CO peak (m/z = 29) and mass spectra for the photocatalytic $^{13}CO_2$ reduction system are presented in Fig. S5. After the completion of the reaction, the mass spectra shows dominant peaks of m/z = 45 ($^{13}CO_2$) and m/z = 29 (^{13}CO) with no peak for ^{12}CO (m/z = 28) observed. Corresponding to this, a ^{13}CO peak (m/z = 29) observed in the gas chromatogram. The results point to the formation of ^{13}CO and provides direct evidence that the

origin of the evolved CO is indeed from the reduction of CO_2 itself. The kinetic study (Fig. 4b) shows a constant CO evolution rate over a 6-hour testing period, which shows that the catalyst maintained its photoactivity throughout the course of the reaction. The O-containing groups of the BNO QDs, particularly the OB_3 centres, likely played a dominant role in the photochemistry of the material[43].

In conclusion, we proposed a one-step hydrothermal route to synthesise photoactive boron oxynitride quantum dots. This approach transformed the material from a wide band gap insulator to a UV-light harvesting n-type semiconductor. For the first time, it was demonstrated that BNO QDs are able to facilitate gas phase CO_2 photoreduction, in a simple solid/gas phase setup, under ambient conditions without the presence of a co-catalyst. The evolution rate exceeded that of P25 TiO_2 (*i.e.* – the benchmark catalyst in the field). These BNO QDs represent a step change and a new design paradigm to the existing BN photocatalyst family.

Conflicts of interest

There are no conflicts to declare.

References

1. X. Wang, G. Sun, N. Li and P. Chen, *Chem. Soc. Rev.*, 2016, **45**, 2239-2262.
2. Y. R. Kumar, K. Deshmukh, K. K. Sadasivuni and S. K. Pasha, *RSC Adv.*, 2020, **10**, 23861-23898.
3. M. J. Molaei, *Solar Energy*, 2020, **196**, 549-566.
4. S. Radhakrishnan, J. H. Park, R. Neupane, C. A. de los Reyes, P. M. Sudeep, M. Paulose, A. A. Martí, C. S. Tiwary, V. N. Khabashesku and O. K. Varghese, *Part. Part. Syst. Charact.*, 2019, **36**, 1800346.
5. S. C. Dhanabalan, B. Dhanabalan, J. S. Ponraj, Q. Bao and H. Zhang, *Adv. Opt. Mater.*, 2017, **5**, 1700257.
6. K. V. Vokhmintcev, P. S. Samokhvalov and I. Nabiev, *Nano Today*, 2016, **11**, 189-211.
7. D. S. Achilleos, H. Kasap and E. Reisner, *Green Chem.*, 2020, **22**, 2831-2839.
8. Y. Bao, J. Wang, Q. Wang, X. Cui, R. Long and Z. Li, *Nanoscale*, 2020, **12**, 2507-2514.
9. T. Uekert, M. F. Kuehnel, D. W. Wakerley and E. Reisner, *Energy Environ. Sci.*, 2018, **11**, 2853-2857.
10. B. C. Martindale, G. A. Hutton, C. A. Caputo, S. Prantl, R. Godin, J. R. Durrant and E. Reisner, *Angew. Chem.*, 2017, **129**, 6559-6563.
11. F. Qiu, Z. Han, J. J. Peterson, M. Y. Odoi, K. L. Sowers and T. D. Krauss, *Nano Lett.*, 2016, **16**, 5347-5352.
12. L. Wang, R. Fernández-Terán, L. Zhang, D. L. Fernandes, L. Tian, H. Chen and H. Tian, *Angew. Chem. Int. Ed.*, 2016, **55**, 12306-12310.
13. X. Xiang, B. Zhu, B. Cheng, J. Yu and H. Lv, *Small*, 2020, **16**, 2001024.
14. Q. Zhang, F. Yang, S. Zhou, N. Bao, Z. Xu, M. Chaker and D. Ma, *Appl. Catal. B*, 2020, **270**, 118879.
15. M. M. Fiume, W. F. Bergfeld, D. V. Belsito, R. A. Hill, C. D. Klaassen, D. C. Liebler, J. G. Marks Jr, R. C. Shank, T. J. Slaga and P. W. Snyder, *Int. J. Toxicol*, 2015, **34**, 53S-60S.
16. D. Krepel, L. Kalikhman-Razvozov and O. Hod, *J. Phys. Chem. C*, 2014, **118**, 21110-21118.

17. S. S. Yamijala, A. Bandyopadhyay and S. K. Pati, *J. Phys. Chem. C*, 2013, **117**, 23295-23304.
18. S. Angizi, F. Shayeganfar, M. H. Azar and A. Simchi, *Ceram. Int.*, 2020, **46**, 978-985.
19. B. Huo, B. Liu, T. Chen, L. Cui, G. Xu, M. Liu and J. Liu, *Langmuir*, 2017, **33**, 10673-10678.
20. M. Liu, Y. Xu, Y. Wang, X. Chen, X. Ji, F. Niu, Z. Song and J. Liu, *Adv. Opt. Mater.*, 2017, **5**, 1600661.
21. L. Lin, Y. Xu, S. Zhang, I. M. Ross, A. C. Ong and D. A. Allwood, *Small*, 2014, **10**, 60-65.
22. S. Singh, M. Garg, R. Rani and A. Sharma, *Faraday Discuss.*, 2020, DOI: https://doi.org/10.1039/C9FD00111E.
23. D. Peng, L. Zhang, F.-F. Li, W.-R. Cui, R.-P. Liang and J.-D. Qiu, *ACS Appl. Mater. Interfaces*, 2018, **10**, 7315-7323.
24. J.-H. Jung, M. Kotal, M.-H. Jang, J. Lee, Y.-H. Cho, W.-J. Kim and I.-K. Oh, *RSC Adv.*, 2016, **6**, 73939-73946.
25. Q. Xue, H. Zhang, M. Zhu, Z. Wang, Z. Pei, Y. Huang, Y. Huang, X. Song, H. Zeng and C. Zhi, *RSC Adv.*, 2016, **6**, 79090-79094.
26. Y. Yang, C. Zhang, D. Huang, G. Zeng, J. Huang, C. Lai, C. Zhou, W. Wang, H. Guo and W. Xue, *Appl. Catal. B*, 2019, **245**, 87-99.
27. J. Liu, H. Wang and M. Antonietti, *Chem. Soc. Rev.*, 2016, **45**, 2308-2326.
28. R. B. Shankar, D. Lubert-Perquel, E. Mistry, I. Nevjestic, S. Heutz and C. Petit, *ChemRXiV Preprint*, 2020, DOI: https://doi.org/10.26434/chemrxiv.12333314.v1.
29. R. Shankar, M. Sachs, L. Francàs, D. Lubert-Perquel, G. Kerherve, A. Regoutz and C. Petit, *J. Mater. Chem. A*, 2019, **7**, 23931-23940.
30. Q. Weng, D. G. Kvashnin, X. Wang, O. Cretu, Y. Yang, M. Zhou, C. Zhang, D. M. Tang, P. B. Sorokin and Y. Bando, *Adv. Mater.*, 2017, **29**, 1700695.
31. C. T. Rueden, J. Schindelin, M. C. Hiner, B. E. DeZonia, A. E. Walter, E. T. Arena and K. W. Eliceiri, *BMC Bioinform.*, 2017, **18**, 529.
32. F. Chassagneux, T. Epicier, P. Toutois, P. Miele, C. Vincent and H. Vincent, *J. Eur. Ceram. Soc*, 2002, **22**, 2415-2425.
33. J. Y. Choi, S. J. L. Kang, O. Fukunaga, J. K. Park and K. Eun, *J. Am. Ceram. Soc.*, 1993, **76**, 2525-2528.
34. R. Geick, C. Perry and G. Rupprecht, *Phys. Rev.*, 1966, **146**, 543.
35. A. Kainthola, K. Bijalwan, S. Negi, H. Sharma and C. Dwivedi, *Mater. Today Proc.*, 2020, **28**, 138-140.
36. Y. Han, Y. Niu, M. Liu, F. Niu and Y. Xu, *J. Mater. Chem. B*, 2019, **7**, 897-902.
37. J. Coates, *Interpretation of infrared spectra, a practical approach*, 2006.
38. B. Liu, S. Yan, Z. Song, M. Liu, X. Ji, W. Yang and J. Liu, *Chem. Eur. J*, 2016, **22**, 18899-18907.
39. P. Dibandjo, L. Bois, F. Chassagneux, J. Letoffe and P. Miele, *J. Porous Mater.*, 2008, **15**, 13-20.
40. J. Riviere, Y. Pacaud and M. Cahoreau, *Thin Solid Films*, 1993, **227**, 44-53.
41. K. Watanabe, T. Taniguchi and H. Kanda, *Nat. Mater*, 2004, **3**, 404-409.
42. M. Marszewski, S. Cao, J. Yu and M. Jaroniec, *Mater. Horiz*, 2015, **2**, 261-278.
43. Y. Cao, R. Zhang, T. Zhou, S. Jin, J. Huang, L. Ye, Z. Huang, F. Wang and Y. Zhou, *ACS Appl. Mater. Interfaces*, 2020, **12**, 9935-9943.